AIAA Journal
Vol. 49, No. 2, February 2011

Optimal Hovering Kinematics of Flapping Wings for Micro Air Vehicles

Zaeem A. Khan* and Sunil K. Agrawal†
University of Delaware, Newark, Delaware 19716

DOI: 10.2514/1.J050057

This paper presents theoretical and experimental analyses of insect flapping mechanics and aerodynamics, with the aim of developing flapping-wing micro air vehicles. A model of an insect thorax flapping mechanism is developed that includes a quasi-steady aerodynamic model. Computer simulations of the thorax model show insectlike wing kinematics, including passive wing rotation at the end of the stroke. These kinematics are perturbed in a sequence of experiments using a robotic flapping-wing device to determine optimal hovering kinematics. Experiments are supported with numerical optimization based on the aerodynamic model. Apart from optimal kinematics, this study shows negative aerodynamic power required during wing rotation, which explains passive wing rotation at the end of the stroke.

Nomenclature

C_D	=	cycle-averaged coefficient of drag for the entire wing
C_L	=	cycle-averaged coefficient of lift for the entire wing
C_1	=	coefficient of translational force
C_2	=	coefficient of rotational force
f	=	flapping frequency, $\omega_e/2\pi$, Hz
J_w	=	inertia matrix of the wing, $\mathrm{kg\cdot m^2}$
K_{f1}, K_{f2}	=	parameters of nonlinear flapping spring, $\mathrm{N\cdot m}$
K_{r1}, K_{r2}	=	parameters of nonlinear rotational spring, $\mathrm{N\cdot m}$
$\bar{L}/\bar{D}$	=	cycle-averaged lift-to-drag ratio
$\bar{P}_a$	=	total cycle-averaged aerodynamic power, $\bar{P}_{\mathrm{rot}} + \bar{P}_{\mathrm{flap}}$, W
$\bar{P}_{\mathrm{flap}}$	=	cycle-averaged aerodynamic power required to flap the wing, W
$\bar{P}_{\mathrm{rot}}$	=	cycle-averaged aerodynamic power required to rotate the wing, W
T	=	wing-beat period, $1/f$, s
α_d	=	α^* during downstroke, $\pi/2 - \theta_r^d$, rad
α_u	=	α^* during upstroke, $\pi/2 + \theta_r^u$, rad
α^*	=	constant geometric angle of attack during flapping phase, $\pi/2 - \theta_r^*$, rad
β	=	stroke-plane inclination angle, rad
ΔT	=	fraction of wing-beat period during which the wing rotates, s
δ_T	=	nondimensional parameter used to vary ΔT
Θ_e	=	excitation amplitude, rad
Θ_f	=	amplitude of flapping motion or stroke amplitude, rad
Θ_f^*	=	peak stroke amplitude, rad
θ_e	=	wing excitation angle, rad
θ_f	=	flap angle, rad
θ_r	=	wing rotation angle, rad
θ_r^d	=	θ_r^* during downstroke, rad
θ_f^{ref}	=	reference flapping motion for robotic flapper proportional–integral–derivative controllers
θ_r^{ref}	=	reference rotational motion for robotic flapper proportional–integral–derivative controllers
θ_r^u	=	θ_r^* during upstroke, rad
θ_r^*	=	constant rotation angle during flapping phase or amplitude of rotation, rad
μ_r	=	viscous damping coefficient for rotational motion, $\mathrm{N\cdot(m\cdot s)}$
ρ	=	density of the air, $\mathrm{kg/m^3}$
ϕ_r	=	phase between flapping and rotational motions, deg
$\bar{\omega}$	=	wing angular velocity vector
ω_e	=	excitation frequency or flapping frequency, rad/s

I. Introduction

FLAPPING-WING micro air vehicles (FWMAVs) represent an emerging class of aerial vehicles that can be used as aerial platforms for numerous applications. These include searching for survivors in burning buildings and under collapsed structures, chemical sensing in industry and hazardous environments, inspection of industrial plants and building security, etc. Inspired by the sophisticated biological designs of insects and hummingbirds, FWMAVs are expected to show similar aerial maneuverability. The recent success of the microscale robotic insect experiment brings us closer to achieving this goal [1].

To fulfill these missions, FWMAVs are required to satisfy some key design requirements. One of the most important requirement is energetically efficient hovering, which requires determination of optimal wing kinematics. In the past, optimal hovering-wing kinematics of insects have been studied using experiments and numerical optimization. Sane and Dickinson [2] conducted experiments using dynamically scaled wings to determine the optimal wing kinematics of a fruit fly at a Reynolds number range of 100–200. Berman and Wang [3] investigated energy-minimizing kinematics of three insects (fruit fly, bumblebee, and hawkmoth) using a quasi-steady aerodynamic model and numerical optimization. In these studies, the wing kinematics were approximated by sinusoids, smoothed triangular waveforms, and trapezoidal waveforms. However, wing kinematics of insects differ from these waveforms [4–7]. In insects, the thorax actuation mechanism combined with the elasticity of the wing structure is responsible for the peculiar wing kinematics. In addition, the elastic design of the thorax also plays a role in minimizing power during hovering by storing the wing kinetic energy as strain energy in the thorax exoskeleton [5,8].

In this paper, we determine the optimal wing kinematics that maximize aerodynamic performance during hovering flight. To get a

Received 12 July 2009; revision received 19 April 2010; accepted for publication 5 September 2010.

*Ph.D. Student, Mechanical Systems Laboratory, Department of Mechanical Engineering; Member AIAA.

†Professor, Department of Mechanical Engineering; Director, Mechanical Systems Laboratory.

better understanding of how insect wing motion is generated, we developed a simplified dynamical model of the *Diptera* thorax, which has been studied in detail [9,10]. The thorax model is coupled with a quasi-steady aerodynamic model based on blade element method. Numerical simulation of the model generates insectlike wing kinematics. We parameterized these kinematics and used these parameters in the optimization process. The parameterization allows us to vary the wing motion without changing it qualitatively. In the optimization process, we conduct several experiments on dynamically scaled wings driven by a robotic device. In each experiment, the wing kinematics parameters are perturbed in order to find the optimal values of these parameters to achieve peak aerodynamic performance. The criterion for aerodynamic performance is high lift at a high lift-to-drag ratio averaged over one wing-beat cycle. Numerical optimization based on the quasi-steady aerodynamic model is also used to search for the optimal solution. The ultimate aim of this research is to develop a hummingbird-sized FWMAV operating at a high Reynolds number range (10,000 to 20,000), for which the aerodynamic data are very scarce. Therefore, all experiments and numerical computation are conducted in this Reynolds number range. Another motivation behind this research is to develop flapping mechanisms based on the thorax model in order to mimic the energy-storage capabilities. We anticipate that these mechanisms could be tuned to generate the optimal wing kinematics determined in this paper.

The organization of this paper is as follows: Sec. II, describes in detail the derivation of the thorax model, including kinematics, dynamics, and aerodynamic modeling of flapping wings. Section III describes the experimental setup and methodology as well as experimental verification of the aerodynamic model. Section IV presents the results of aerodynamic tests designed to seek the optimal wing kinematics. Section V investigates the feasibility of passive wing rotation based on experimental results. Finally, Sec. VI presents conclusions and the next phase of this research.

II. Model of Insect Thorax

A. Background and Motivation

The insect thorax consists of a highly elastic exoskeleton made up of chitin microfibers embedded in a protein matrix. This fibrous composite material has the ability to absorb energy and is very strong [11]. The working of an insect flapping mechanism is shown in Fig. 1. The thorax consists of two sets of flight muscles: dorsoventral muscles and longitudinal muscles. These muscles contract alternately and move the roof of the thorax (tergal plate) up and down at high frequency. This linear motion is translated into flapping motion of the wing through a hinge mechanism, as shown in Figs. 1b and 1c.

As the wings approach the end of each stroke, the kinetic energy of the wing is stored as strain energy, due to deformation of the thorax cuticle [11]. The flapping motion of the wing is denoted by θ_f, and θ_e is the excitation angle or the flap angle, assuming a rigid thorax. The difference of $\theta_f - \theta_e$ is proportional to the strain energy. The elastic design of the thorax allows large stroke amplitudes and minimizes the repeated shocks of the beating wing. The flapping motion occurs in a plane called the *stroke plane*, as shown in Fig. 1d.

As the wing flaps, it twists passively along the span near the end of each stroke, due to the aerodynamic and inertial forces. In small insects, such as honeybees and fruit flies, the twist occurs very close to the wing base. The rest of the wing rotates like a rigid body by an angle θ_r (rotation angle), as shown in Fig. 1d. Insect wings have remarkable built-in structural mechanisms to prevent the wing from rotating beyond a rotation angle θ_r^*. This is related to the geometric angle of attack $\alpha^* = \pi/2 - \theta_r^*$. As the wing flips and approaches θ_r^*, the rotational stiffness increases sharply and maintains α^* during the flapping phase of the motion [12]. The wing motion of a honeybee in Fig. 2 shows nearly sinusoidal flapping motion, whereas the rotational motion is nearly flat on top and marked by overshoots, due to the sharp increase of rotational stiffness as α^* is reached. The thorax excites another mode shape, called the deviation angle θ_d, which takes the wing out of the stroke plane, as shown in Fig. 1e. However, θ_d is typically much smaller than θ_f and θ_r and is therefore ignored in this study [2,4,5].

B. Mathematical Modeling

To model the thorax, the flight muscles are replaced by an actuator that can provide the excitation by oscillation, as shown in Fig. 3a. The elastic thorax exoskeleton is modeled as a nonlinear spring that connects the flight muscles to the wing hinge. This spring is referred as the flapping spring. The elastic twist of the wing near the base is modeled by another nonlinear spring, referred as the rotational spring. The wing is assumed to be rigid; therefore, the system has two

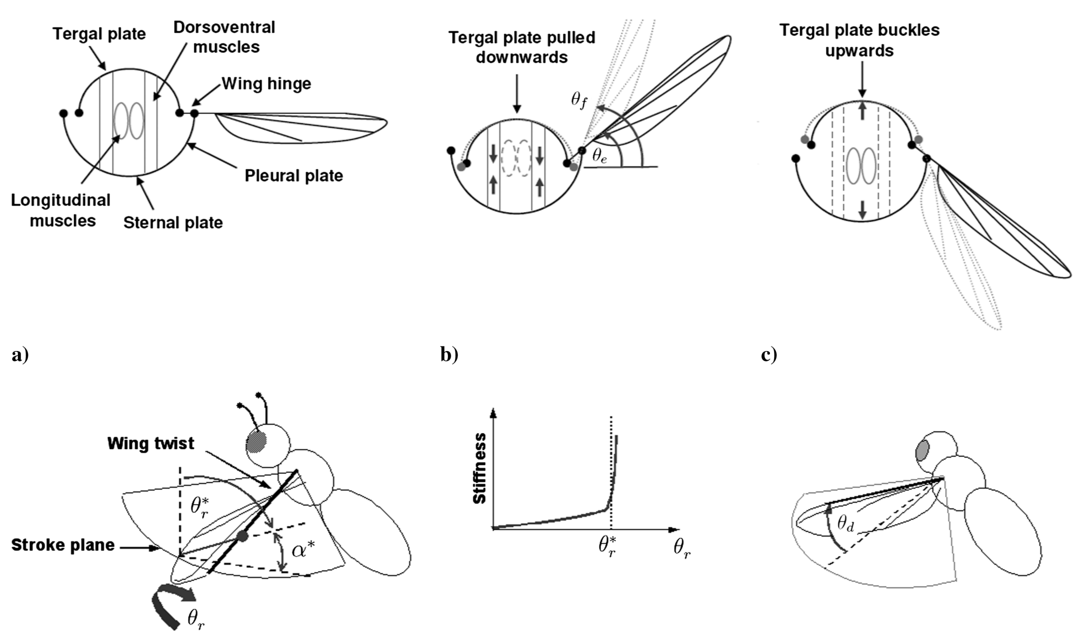

Fig. 1 Schematics of an insect thorax flapping mechanism: a) parts of the thorax, including the main flight muscles; b–c) flapping motion is generated by up and down oscillations of the tergal plate (tergal plate deformation is shown in light gray); d) rotational motion is generated passively by aerodynamic and inertial loads causing the wing to twist near the base; and e) out of stroke plane or deviation angle θ_d.

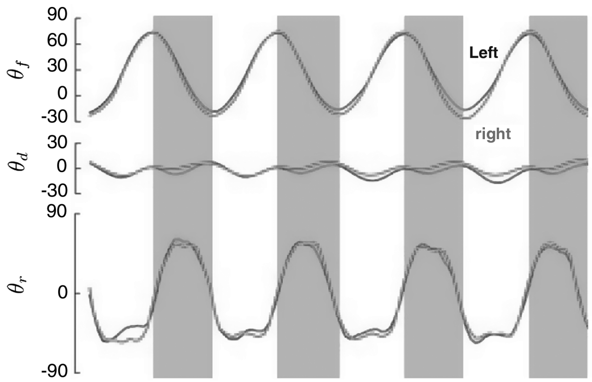

Fig. 2 Honeybee wing motion trajectories for both left and right wings. (Figure is modified from [4] and reprinted with permission from the National Academy of Sciences.)

degrees of freedom (θ_f, θ_r). This is a simplified representation of the complex insect wing motion that has infinite degrees of freedom. We attach a coordinate system to the rigid wing of $\mathcal{F}_w$: $(\hat{x}_w, \hat{y}_w, \hat{z}_w)$, as shown in Fig. 3b, with the origin denoted by B at the wing base. The $\hat{x}_w$ axis is normal to the wing surface, $\hat{y}_w$ is along the spanwise direction along the wing leading edge, and $\hat{z}_w$ is along the chordwise direction.

1. *Wing Kinematics*

This analysis assumes that the insect body is fixed in space. Therefore, the inertial frame $\mathcal{F}_o$: $(\hat{x}_o, \hat{y}_o, \hat{z}_o)$ shown in Fig. 3c is also the body frame. The unit vectors $(\hat{x}_o, \hat{y}_o)$ describe a horizontal plane parallel to the Earth, $\hat{y}_o$ is normal to the plane of symmetry of an insect body, and $\hat{z}_o$ is along the gravity direction. The wing frame $\mathcal{F}_w$ can be described by three successive rotations with respect to the inertial frame $\mathcal{F}_o$: $(\hat{x}_o, \hat{y}_o, \hat{z}_o)$, as shown in Figs. 3c–3e. First, rotation about the $\hat{y}_o$ axis by an angle β; second, a rotation about the current $\hat{z}_s$ axis by θ_f; and third, rotation about the current $\hat{y}_1$ axis about the leading edge by θ_r. We refer to $\hat{z}_s$ as the *flapping axis* and to $\hat{y}_w$ as the *rotational axis* of the wing. The frame $\mathcal{F}_s$: $(\hat{x}_s, \hat{y}_s, \hat{z}_s)$ is referred to as the *stroke-plane frame,* and $(\hat{x}_s, \hat{y}_s)$ describes the stroke plane. The angle β gives the tilt of the stroke plane with respect to the horizontal $(\hat{x}_o, \hat{y}_o)$ plane and is varied by insects for flight control [5]. For steady hovering, β is a constant parameter. The rotation matrix between $\mathcal{F}_o$ and $\mathcal{F}_s$ is denoted by R_o^s, between $\mathcal{F}_s$ and $\mathcal{F}_1(\hat{x}_1, \hat{y}_1, \hat{z}_1)$ is denoted by R_s^1, and between $\mathcal{F}_1$ and $\mathcal{F}_w$ is denoted by R_1^w. These are given by

$$R_o^s = \begin{pmatrix} C_\beta & 0 & S_\beta \\ 0 & 1 & 0 \\ -S_\beta & 0 & C_\beta \end{pmatrix}, \qquad R_s^1 = \begin{pmatrix} C_{\theta_f} & -S_{\theta_f} & 0 \\ S_{\theta_f} & C_{\theta_f} & 0 \\ 0 & 0 & 1 \end{pmatrix}$$

$$R_1^w = \begin{pmatrix} C_{\theta_r} & 0 & S_{\theta_r} \\ 0 & 1 & 0 \\ -S_{\theta_r} & 0 & C_{\theta_r} \end{pmatrix} \tag{1}$$

where symbols C_β and S_β represent $\cos\beta$ and $\sin\beta$, respectively. Similar representations are used for the other angles. The angular velocity of the wing in the wing frame is given by

$$\bar{\omega} = -\dot{\theta}_f \sin\theta_r \hat{x}_w + \dot{\theta}_r \hat{y}_w + \dot{\theta}_f \cos\theta_r \hat{z}_w \tag{2}$$

The wing motion can be divided into two phases. The first is a flapping phase during which $\dot{\theta}_r \sim 0$ and the wing maintains nearly constant rotation angle θ_r^*, corresponding to the angle of attack $\alpha^* = \pi/2 - \theta_r^*$. The second is a rotational phase near the end of the stroke, during which the wing flips in order to set α^* for the subsequent stroke.

2. *Aerodynamic Model*

In this paper, we used a quasi-steady aerodynamic model based on blade element method. The wing is divided into N elements, or strips. from the base to the tip of the wing. The differential aerodynamic force is computed for each strip and then integrated to obtain the total force. During the flapping phase, a vortex is created above the leading edge, which significantly increases circulation (and, consequently, the lift force) in insects [13,14]. In scaled hawkmoth wings revolving at constant speed, this leading-edge vortex (LEV) remains attached, and a constant circulation and aerodynamic force are maintained [15]. Furthermore, the resultant force due to the LEV remains normal to the wing surface, due to the dominance of pressure forces [15]. As the wing rotates near the end of the stroke, a rotational circulation force is generated [16]. Finally, as the wing accelerates from rest at the end of the stroke, it experiences apparent mass force and wake-capture effects [11,17]. The major contribution comes from the normal LEV force during the flapping phase, and we therefore assume that the aerodynamic force remains normal to the wing throughout the wing beat. The differential normal force vector on the ith wing element with a cord length c_i and width $\mathrm{d}r_i$ is given by

$$\overline{\mathrm{d}F}_i = \mathrm{d}F_i \hat{x}_w = (C_1(\alpha_i)\tfrac{\rho}{2}|\bar{V}_i|^2 c_i\, \mathrm{d}r_i)\hat{x}_w \tag{3}$$

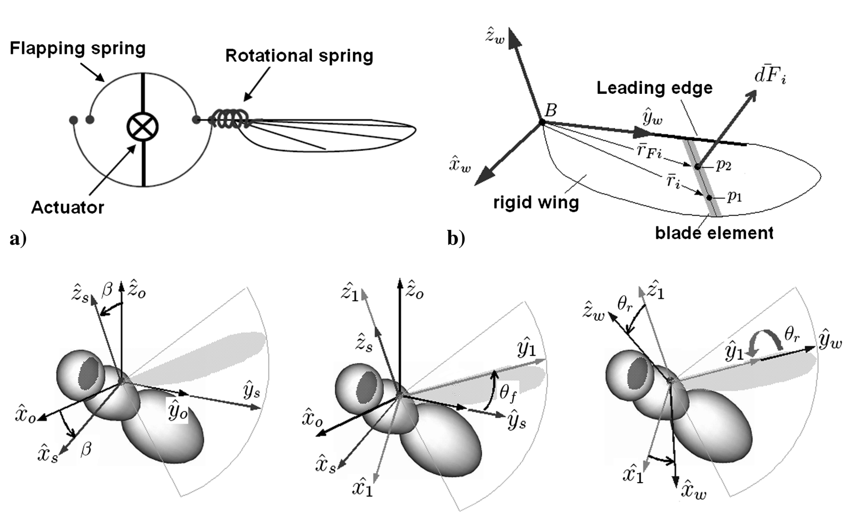

Fig. 3 Schematics of a) simplified insect thorax model with thorax muscles replaced by an actuator; b) coordinate frame $\mathcal{F}_w$: $(\hat{x}_w, \hat{y}_w, \hat{z}_w)$ is attached to the rigid wing; c–e) sequence of three rotations (β, θ_f, and θ_r) that describe the stroke-plane inclination and wing motion.

where $C_1(\alpha_i)$ is a coefficient of normal LEV force, which is a function of angle of attack α_i of the ith element; ρ is the density of the air; and $\bar{V}_i = V_{ix}\hat{x}_w + V_{iz}\hat{z}_w$ is the flow velocity vector. The spanwise component V_{iy} along $\hat{y}_w$ axis is ignored, since it does not contribute to the aerodynamic force. According to Walker [17], the rotational force can be computed along with the LEV force by evaluating $\bar{V}_i$ at a location p_1 along the chord at each blade element, as shown in Fig. 3b. The expression for $\bar{V}_i$ is given by

$$\begin{aligned}|\bar{V}_i|^2 &= |\bar{\omega} \times \bar{r}_i|^2 = V_{ix}^2 + V_{iz}^2 \\ &= C_2^2 c_i^2 \dot{\theta}_r^2 + 2C_2\dot{\theta}_r\dot{\theta}_f \cos\theta_r r_i c_i + r_i^2\dot{\theta}_f^2 \end{aligned} \tag{4}$$

where $\bar{\omega}$ is the angular velocity vector of the wing, given by Eq. (2); $\bar{r}_i = r_i\hat{y}_w - C_2c_i\hat{z}_w$ is the position vector from the base B to the point p_1; and C_2c_i is the distance from the leading edge ($\hat{y}_w$ axis) to point p_1 along the ith blade element, as shown in Fig. 3b. The parameter C_2 is a nondimensional coefficient of rotational force. If we substitute the expression for $|\bar{V}_i|^2$ in Eq. (3) and integrate for the entire wing, we get the total aerodynamic force vector on a rigid wing as

$$\begin{aligned}\bar{F}_a = F_x\hat{x}_w = \sum_{i=1}^{N} \mathrm{d}F_i\hat{x}_w = \{C_1(\alpha_i)F_1(\dot{\theta}_f) \\ + F_2[C_1(\alpha_i), C_2, \dot{\theta}_f, \dot{\theta}_r]\}\hat{x}_w\end{aligned} \tag{5}$$

where

$$F_x = \sum_{i=1}^{N} \mathrm{d}F_i$$

Here, the orthogonal components F_y and F_z are zero, since $\bar{F}_a$ is assumed to be normal to the wing. The functions F_1 and F_2 capture the LEV and rotational forces, respectively, and the coefficients C_1 and C_2 adjust the magnitude of the two terms. The function F_2 depends upon both C_1 and C_2. These functions are given by

$$F_1 = \frac{\rho}{2}\dot{\theta}_f|\dot{\theta}_f| \sum_{i=1}^{N} r_i^2 c_i \,\mathrm{d}r_i \tag{6}$$

$$\begin{aligned}F_2 = \frac{\rho}{2}\Bigg(\dot{\theta}_r^2 \sum_{i=1}^{N} C_1(\alpha_i)C_2^2c_i^3 \,\mathrm{d}r_i \\ + 2\dot{\theta}_r\dot{\theta}_f \cos\theta_r \sum_{i=1}^{N} C_1(\alpha_i)C_2 r_i c_i^2 \,\mathrm{d}r_i\Bigg)\end{aligned} \tag{7}$$

The virtual mass force can be modeled and added as $C_3F_3(\dot{\theta}_f, \dot{\theta}_r, \ddot{\theta}_f, \ddot{\theta}_r)$ in Eq. (5). However, this effect is minimal and is therefore neglected in this study. The unknown coefficients are determined using experimental data; this is explained in Sec. III. $\bar{F}_a$ can be transformed in the inertial frame $\mathcal{F}_o$ and frame $\mathcal{F}_1$ as follows:

$$\begin{pmatrix} F_h \\ F_l \\ F_v \end{pmatrix}_o = R_o^s R_s^1 R_1^w \bar{F}_a, \qquad \begin{pmatrix} D \\ 0 \\ L \end{pmatrix}_1 = R_1^w \bar{F}_a \tag{8}$$

where F_h is the horizontal component in the $\hat{x}_o$ direction, F_l is the lateral component in the $\hat{y}_o$ direction, and F_v is the vertical component in the $\hat{z}_o$ direction. In frame $\mathcal{F}_1$, L and D are the total lift and drag forces normal and parallel to the stroke plane along the $\hat{z}_1$ and $\hat{x}_1$ directions, respectively. The aerodynamic moment vector at the wing base B is given by

$$\begin{aligned}\bar{M}_a^B = \sum_{i=1}^{N} \bar{r}_{Fi} \times \overline{\mathrm{d}F}_i = \left(-C_{my}\sum_{i=1}^{N} c_i \,\mathrm{d}F_i\right)\hat{y}_w \\ + \left(-\sum_{i=1}^{N} r_i \,\mathrm{d}F_i\right)\hat{z}_w = M_y\hat{y}_w + M_z\hat{z}_w\end{aligned} \tag{9}$$

where $\bar{r}_{Fi} = C_{my}c_i\hat{y}_w - r_i\hat{z}_w$ is a position vector from the wing base B to the point p_2, where $\overline{\mathrm{d}F}_i$ acts on each blade element, as shown in Fig. 3b. The parameter C_{my} is the percentage of chord distance from the leading edge to point p_2. The component of aerodynamic moment about the $\hat{y}_w$, or rotational, axis is $M_y = M_y(\dot{\theta}_f, \dot{\theta}_r)$, and the component of moment about the $\hat{z}_w$ axis is $M_z = M_z(\dot{\theta}_f, \dot{\theta}_r)$. The M_x component of the moment is zero, since $\overline{\mathrm{d}F}_i$ is assumed to act normal to the chord. The aerodynamic power is given by

$$\begin{aligned}P_a = \bar{M}_a^B \cdot \bar{\omega} = M_y\omega_y + M_z\omega_z = \left(-C_{my}\sum_{i=1}^{N} c_i \,\mathrm{d}F_i\right)\dot{\theta}_r \\ + \left(-\sum_{i=1}^{N} r_i \,\mathrm{d}F_i\right)\dot{\theta}_f \cos\theta_r\end{aligned} \tag{10}$$

where ω_y and ω_z are the components of $\bar{\omega}$ given by Eq. (2), $M_y\omega_y$ is the power required to rotate the wing (P_{rot} is rotational power), and $M_z\omega_z$ is the power required to flap the wing (P_{flap} is flapping power).

3. *Equations of Motion*

The equations of motion of the thorax model are derived based on Lagrange's equations with $q = (\theta_f, \theta_r)^T$ as the generalized coordinate vector. The equations are given by

$$\frac{\mathrm{d}}{\mathrm{d}t}\left(\frac{\partial \mathcal{T}}{\partial \dot{q}}\right)^T - \left(\frac{\partial \mathcal{T}}{\partial q}\right)^T + \left(\frac{\partial \mathcal{V}}{\partial q}\right)^T = Q \tag{11}$$

where $\mathcal{V}$ is the potential energy, Q is the generalized force vector, and $\mathcal{T}$ is the kinetic energy given by

$$\mathcal{T} = \frac{1}{2}\bar{\omega}^T J_w \bar{\omega}, \qquad J_w = \begin{pmatrix} J_x & 0 & 0 \\ 0 & J_y & J_{yz} \\ 0 & J_{yz} & J_z \end{pmatrix}_B \tag{12}$$

where $\bar{\omega}$ is given by Eq. (2) and J_w is the wing inertial matrix in the $\mathcal{F}_w$ frame computed at the wing base B. The potential energy is given by

$$\begin{aligned}\mathcal{V} = \tfrac{1}{2}K_{f1}(\theta_e - \theta_f)^2 + \tfrac{1}{4}K_{f2}(\theta_e - \theta_f)^4 + \tfrac{1}{2}K_{r1}\theta_r^2 \\ + \tfrac{1}{4}K_{r2}\theta_r^4 + \tfrac{1}{2}K_{r3}\theta_r^2\end{aligned} \tag{13}$$

where θ_e is the excitation angle; K_{f1} and K_{f2} are parameters of the nonlinear flapping spring; and K_{r1}, K_{r2}, and K_{r3} are parameters of the nonlinear rotational spring. The additional parameter K_{r3} is a discontinuous function of θ_r. It is included to model the sharp increase in rotational stiffness in an insect wing, as shown in Fig. 1d. Mathematically, K_{r3} is given by

$$K_{r3}(\theta_r, \theta_r^*) = \begin{cases} 0 & \text{if } |\theta_r| < \theta_r^* \\ K_{r3} & \text{if } |\theta_r| \geq \theta_r^* \end{cases} \tag{14}$$

Note that in order to maintain α^*, then $K_{r3} \gg K_{r1}, K_{r2}$. The virtual work is given by

$$\delta W = \bar{M}_a^B \cdot \delta\bar{\omega} - \mu_r\dot{\theta}_r \cdot \delta\theta_r \tag{15}$$

where $\delta\bar{\omega}$ is the variation of wing angular velocity vector $\bar{\omega}$, and μ_r is the viscous damping coefficient for the rotational motion. The equation of motion of the coupled oscillator system is given by

$$M(q)\ddot{q} + C(q, \dot{q}) + G(q) = Q(q, \dot{q}) \tag{16}$$

where the inertial matrix $M(q)$, centrifugal force vector $C(q, \dot{q})$ potential force vector $G(q)$, and generalized force vector $Q(q, \dot{q})$ are given by

$$M(q) = \begin{pmatrix} \sin^2\theta_r J_x + \cos^2\theta_r J_z & \cos\theta_r J_{yz} \\ \cos\theta_r J_{yz} & J_y \end{pmatrix}$$

$$C(q,\dot{q}) = \begin{pmatrix} (J_x - J_z)\sin(2\theta_r)\dot{\theta}_f\,\dot{\theta}_r - J_{yz}\sin\theta_r\dot{\theta}_r{}^2 \\ -\frac{1}{2}(J_x - J_z)\sin(2\theta_r)\dot{\theta}_f{}^2 \end{pmatrix}$$

$$G(q) = \begin{pmatrix} -K_{f1}(\theta_e - \theta_f) - K_{f2}(\theta_e - \theta_f)^3 \\ K_{r1}\theta_r + K_{r2}\theta_r^3 + K_{r3}\theta_r \end{pmatrix}$$

$$Q(q,\dot{q}) = \begin{pmatrix} \cos\theta_r M_z(\dot{\theta}_f, \dot{\theta}_r) + \tau_d \\ M_y(\dot{\theta}_f, \dot{\theta}_r) - \mu_r\dot{\theta}_r \end{pmatrix}$$

where $Q(q,\dot{q})$ is obtained from Eq. (15). The system is excited by $\theta_e(t) = \Theta_e\cos(\omega_e t)$ in the $G(q)$ vector. The dynamic Eq. (16) along with the aerodynamic model given by Eq. (5) constitutes the complete model of the system.

C. Computer Simulation

The result of numerical simulation of Eq. (16) is shown in Fig. 4 after the system attains steady state. Note that the rotational motion is qualitatively similar to the honeybee wing motion shown in Fig. 2. Also note that θ_f trajectory is not exactly a sinusoid. The trajectory is curved on one side and straight on the other side, as indicated in Fig. 4. The honeybee flapping motion has a similar profile (see the θ_f trajectory in Fig. 2). This motion can be described by a few parameters that allow variation in kinematics without changing it qualitatively. As shown in Fig. 4, these parameters are the stroke amplitude Θ_f; the constant geometric angle of attack $\alpha^* = \pi/2 - \theta_r^*$, which can be further divided into angle of attack during upstroke α_u and downstroke α_d; the duration of wing rotation ΔT, which is a fraction of wing-beat time period T during which flip occurs; the phase shift ϕ_r between the flapping and rotational motions; and the inclination of the stroke plane β. In the next sections, the optimal set $\{\Theta_f, \alpha_u, \alpha_d, \phi_r, \Delta T, \beta\}$ is determined based on maximum aerodynamic performance.

III. Experimental Methodology

A. Robotic Flapper

To characterize the aerodynamics of flapping wings, a robotic flapper was designed and fabricated (Fig. 5). It consists of two independent servo motors that move a scaled-up wing according to the desired flapping and rotational motions. A force-torque sensor (Nano17 from ATI Industrial Automation) is mounted near the wing base. The sensor captures all three components of forces and moments as the wing moves. These data are filtered online using a first-order filter and filtered offline using a zero-phase-delay low-pass Butterworth filter with a cutoff frequency set to 15 times the flapping frequency of the robotic flapper. The gravity and inertial loads of the wing are computed online using a Newton–Euler equation and subtracted from the sensor output to get the pure aerodynamic force and torque, which are transformed into the wing frame $\mathcal{F}_w$ (Fig. 5). The resolution of the sensor is 0.0031 N for the forces and 0.0156 N · mm for the moments.

A steady-state solution of Eq. (16) can be used as a reference signal for the servo motor proportional–integral–derivative (PID) controllers. However, Eq. (16) is highly nonlinear and might result in unexpected motion when certain parameters are changed to vary the kinematics. Therefore, for the safety of the flapper and sensor, the steady-state solution of Eq. (16) is fitted by Fourier series for the

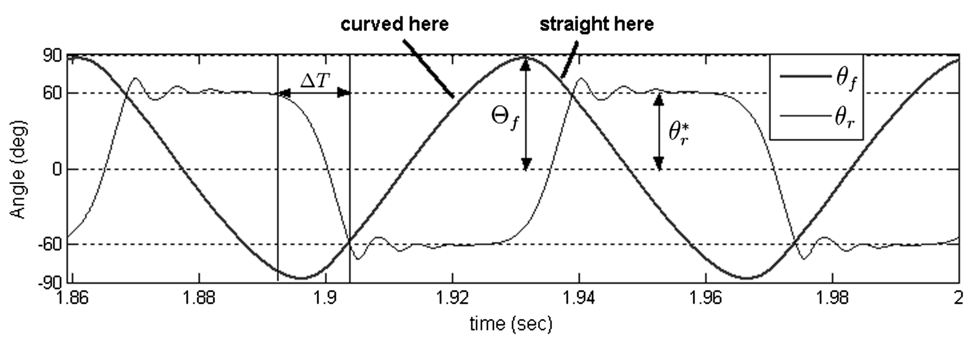

Fig. 4 Typical numerical simulation result of the thorax model after reaching steady state. Here, $\Theta_f \approx 90°$ and $\theta_r^* = 60°$ or $\alpha^* = \pi/2 - \theta_r^* = 30°$. Note that θ_r varies very little from θ_r^* during the flapping phase, due to the presence of K_{r3} term. The system parameters are $J_x = 1.12\text{e} - 5\ \text{kg}\cdot\text{m}^2$, $J_y = 2.24\text{e} - 7\ \text{kg}\cdot\text{m}^2$, $J_z = 1.1\text{e} - 5\ \text{kg}\cdot\text{m}^2$, $J_yz = 8.82\text{e} - 7\ \text{kg}\cdot\text{m}^2$, $K_{f1} = K_{f2} = 0.016\ \text{N}\cdot\text{m}$, $K_{r1} = K_{r2} = 0.0001\ \text{N}\cdot\text{m}$, $K_{r3} = 0.15\ \text{N}\cdot\text{m}$, $\mu_r = 1\text{e} - 5\ \text{N}\cdot(\text{m}\cdot\text{s})$, $\Theta_e = 30°$, and $\omega_e = 57\ \text{rad/s}$.

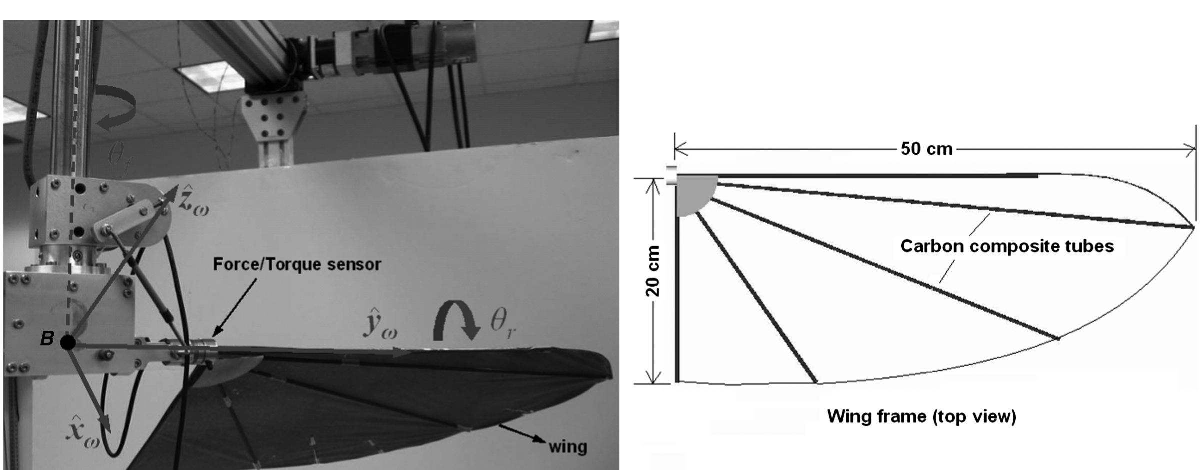

Fig. 5 Robotic flapper designed and fabricated at the University of Delaware. It is driven by independent servo motors to generate (θ_f, θ_r) wing motion. A six-axis sensor records the aerodynamic force and torque loads generated by the wing. These data are transformed into the wing frame $\mathcal{F}_w(\hat{x}_w, \hat{y}_w, \hat{z}_w)$. The wing planform used in all experiments is also shown.

flapping motion and a linear second-order oscillator is used to fit the rotational motion as follows:

$$\theta_f^{\mathrm{ref}}(t) = \sum_{n=1}^{3} c_n \cos(2\pi n f t + \theta_n) \tag{17}$$

$$\ddot{\theta}_r^{\mathrm{ref}}(t) + 30f\dot{\theta}_r^{\mathrm{ref}}(t) + 400f^2\theta_r^{\mathrm{ref}}(t) = 400f^2F(t) \tag{18}$$

where

$$F(t) = \begin{cases} \cos(2\pi f t + \phi_r)\delta_T, & \text{if } \theta_r^u < \cos(2\pi f t + \phi_r)\delta_T < \theta_r^d \\ \theta_r^d & \text{if } \cos(2\pi f t + \phi_r)\delta_T \geq \theta_r^d \\ \theta_r^u & \text{if } \cos(2\pi f t + \phi_r)\delta_T \leq \theta_r^u \end{cases}$$

where c_n is the amplitude, θ_n is the phase of the nth harmonic, f is the flapping frequency of the robotic flapper, and ϕ_r is the phase between flapping and rotational motions. The stroke amplitude can be varied by varying the amplitude of the first harmonic: i.e., $\Theta_f = c_1$. The forcing function $F(t)$ is a clipped sine wave, where the parameter δ_T is used to manipulate ΔT, and θ_r^u and θ_r^d adjust α^u and α^d, respectively. This formulation allows variation of wing kinematics parameters $\{\Theta_f, \alpha_u, \alpha_d, \phi_r, \Delta T, \beta\}$. For the optimization study, we start with the following set of nominal kinematics parameters: $\Theta_f = 70°$, $\alpha_u = \alpha_d = \alpha^* = 35°$, $\phi_r = 0°$, and $\beta = 0°$, and flip duration ΔT is considered nominal, for which $\delta_T = 150$ in Eq. (18).

For hovering flight, lift balances the weight, and the drag should average to zero. Therefore, when $\beta = 0°$, the angle of attack is kept identical during both upstroke and downstroke in order to cancel the wing drag: i.e., $\alpha_u = \alpha_d = \alpha^*$. The PID controllers for the servo motor are tuned to follow $\theta_f^{\mathrm{ref}}(t)$ and $\theta_r^{\mathrm{ref}}(t)$ reference trajectories with a high degree of precision.

B. Dynamic Scaling

The governing equation describing insect aerodynamics is the Navier–Stokes equation. We nondimensionalize the Navier–Stokes equation using the time period T of wing-beat cycle as the time scale, the mean wing tip velocity $U_t = 4f\Theta_f R$ as the velocity scale, and the mean chord as the length scale:

$$\bar{c} = \sum_{i=1}^{N} c_i \frac{\mathrm{d}r_i}{R}$$

where R is the wing length from the wing base B to the wing tip. The nondimensional equation is given by

$$K\frac{\partial \bar{u}}{\partial \tau} + \bar{u}\cdot\nabla\bar{u} = -\nabla\bar{P} + \frac{1}{Re}\nabla^2\bar{u} \tag{19}$$

where the Reynolds number Re and the reduced frequency parameter K are nondimensional parameters given by

$$Re = \frac{4f\Theta_f R\bar{c}}{\nu}, \qquad K = \frac{\bar{c}}{4\Theta_f R} \tag{20}$$

To obtain dynamic scaling, it is necessary to keep the values of both Re and K the same for the flapper wing and a one-fifth-scale FWMAV wing. The scaled-up flapper wing is made from carbon composite tubes and covered with Mylar membrane that is heat-shrunk on to the carbon composite frame. The carbon tubes ensure that the wing structure does not deform under aerodynamic loads. However, the Mylar membrane billows slightly between the tubes, thus changing the wing profile as the wing moves. Furthermore, the membrane is attached on one side of the frame, which causes an asymmetric change in wing profile between upstroke and downstroke.

C. Calibration and Validation of Aerodynamic Model

The aerodynamic model requires the coefficients C_1 and C_2 and the parameter C_{my} [refer to Eqs. (6), (7), and (9)]. The coefficients C_1 and C_2 are determined sequentially, since the functions F_1 and F_2 are partially independent during the wing-beat cycle. During the flapping phase, $F_2 \approx 0$, since $\dot{\theta}_r \approx 0$, and $F_1 \neq 0$ and approaches maximum value near midstroke ($\theta_f = 0$). During the rotational phase, near the end of the stroke, $\dot{\theta}_f \to 0$; consequently, $F_1 \to 0$, whereas F_2 approaches maximum value, because $\dot{\theta}_r$ is maximum. Therefore, during flapping phase, near midstroke,

$$F_x \approx C_1F_1 \Rightarrow C_1(\alpha^*) \approx F_x/F_1$$

where the F_x component is acquired from the sensor, and F_1 is known. Since $\dot{\theta}_r = 0$ near midstroke, $\alpha_i = \alpha^*$ for all wing elements. Therefore, at midstroke, $C_1(\alpha_i) = C_1(\alpha^*)$ and is determined over a range of α^* values from 10 to 90°. Next C_2 is adjusted until the model matches with the sensor data near the end of the stroke. Finally, moment M_y is matched by adjusting the parameter C_{my}. C_1 varies almost linearly with α^* and can be fitted by $C_1(\alpha^*) = (\mathrm{d}C_1/\mathrm{d}\alpha^*)\alpha^*$. For the wing used in our experiment, we found that $\mathrm{d}C_1/\mathrm{d}\alpha^* = 6/\pi \equiv$, $C_2 = 0.65$, and $C_{my} = 0.5$ give the best fit.

A comparison of experimental data and aerodynamic model over one wing-beat cycle is given in Fig. 6 for a typical kinematic pattern. The experimental data are averaged over 10 wing beats and compared with the aerodynamic model and a truncated model C_1F_1. The normal F_x force component and the M_y and M_z moment components of the model match very well with the experimental data during the entire wing-beat cycle. However, the experimental data are not symmetric between the upstroke and downstroke. This is most likely due to asymmetric deflection of the Mylar membrane, as explained in Sec. III.B. The chordwise force component F_z shows a lot of variation over 10 wing beats and remains close to zero. F_z is not identically zero, due to noise in the data caused by minute structural vibrations and asymmetric membrane deflection as the wing moves. Similarly, the M_x component (not shown) is also close to zero. This validates our assumption that the resultant force is normal to the wing. The full model $F_x = C_1F_1 + F_2$ compares very well, and the truncated model $F_x = C_1F_1$ compares well during the flapping phase, but fails to predict the force peaks near the end of the stroke, due to wing rotation. However, these rotational peaks vanish as Θ_f approaches 90°; in that case, $F_x = C_1F_1$ is sufficient to predict the aerodynamic force.

IV. Optimal Hovering Kinematics

A. Performance Criteria

We define the cycle-averaged lift and drag coefficients as follows:

$$C_L = \frac{\frac{1}{T}\int_o^T L(t)\,\mathrm{d}t}{1/2\rho S_2\pi^2(f\Theta_f)^2}, \qquad C_D = \frac{\frac{1}{T}\int_o^T |D(t)|\,\mathrm{d}t}{1/2\rho S_2\pi^2(f\Theta_f)^2} \tag{21}$$

where

$$S_2 = 2\sum_i^N r_i^2 c_i\,\mathrm{d}r_i$$

is the second moment of wing area [5], and the numerators are the cycle-averaged lift $\bar{L}$ and drag $\bar{D}$. The time-varying lift $L(t)$ and drag $D(t)$ forces are transformed from the wing frame using Eq. (8). Drag cancels out during one wing-beat cycle; therefore, the absolute value of drag is considered. The criterion for aerodynamic performance is high C_L at a high $\bar{L}/\bar{D}$ ratio. To determine the peak operating point, we vary each kinematic parameter in the set $\{\Theta_f, \alpha_u, \alpha_d, \phi_r, \Delta T, \beta\}$ in a sequence of experiments designed to find the optimal kinematic parameter set. This is described in the following sections.

B. Experiment 1: Optimal Stroke Amplitude Θ_f

In the first experiment Θ_f is varied from 30 to 90° in 10° increments while keeping the product $f\Theta_f$ constant. This ensures constant Re, U_t, and the denominator of C_L and C_D, whereas reduced frequency K varies inversely with Θ_f. Other kinematic parameters are $\alpha^* = \alpha_u = \alpha_d = 35°$, $\beta = 0°$, $\phi_r = 0°$, and nominal ΔT.

The experimental results presented in Fig. 7 show an increase of $\bar{L}/\bar{D}$ and C_L as Θ_f increases. The $\bar{L}/\bar{D}$ computed from the model shows a similar trend. The time trajectories of $L(t)$ and $D(t)$ for both

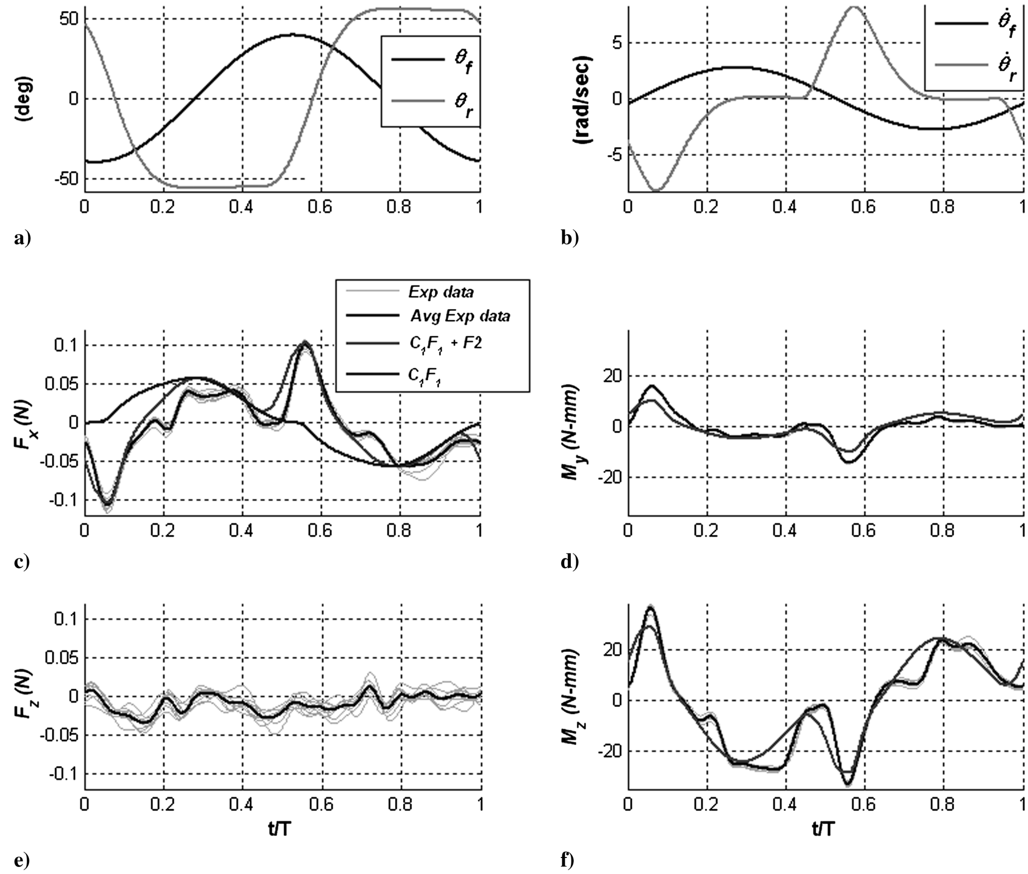

Fig. 6 Comparison of time trajectories of aerodynamic force and torque data with the aerodynamic model: a–b) time trajectories of the actual wing motion obtained from optical rotary encoders, and c–f) aerodynamic data are averaged over 10 wing-beat cycles. The abscissa is the nondimensional time, where t is the actual time and T is the wing-beat period; $Re = 18,326$ and $K = 0.0385$.

experiment and model are shown in Fig. 8 for a range of Θ_f from 30 to 90°. The results show an increase in rotational force peaks due to wing rotation as Θ_f decreases and reduced frequency K increases [see Eq. (20)]. The reduced frequency is a measure of unsteadiness in the flow, as can be seen by Eq. (19). Large values of K indicate greater unsteadiness in the flow. In the case of $\Theta_f = 30°$, K is largest and the data show very large force peaks as well as secondary peaks (indicated by arrows in Fig. 8). This phenomenon is not captured by the quasi-steady aerodynamic model. These peaks decrease the lift and increase the drag. Note that as Θ_f is increased to 90°, the rotational peaks vanish and the aerodynamic force can be predicted by even the truncated model C_1F_1. The results clearly show an increase in aerodynamic performance as Θ_f increases; however, by manipulating rotational motion, aerodynamic performance might be improved even for smaller amplitudes. This leads us to the second experiment.

C. Experiment 2: Optimal Flip Motion

In the second experiment, the wing rotation of flip is varied in two ways from the nominal kinematics:

1) ΔT is varied from nominal to fast and slow, as shown in Fig. 9a.

2) For each ΔT, the phase ϕ_r is varied from $-30°$ (delayed flip) to 30° (advanced flip) in 5° increments, as shown in Fig. 9b.

For this experiment, $\alpha^* = \alpha_u = \alpha_d = 35°$ and $\beta = 0°$. To vary ΔT, the parameter δ_T in Eq. (18) was set to 90, 150, and 3000 for slow, nominal, and fast flip durations, respectively. We perform these experiments at $\Theta_f = 40$ and 90° to see the effect on both small and large amplitudes when the product $f\Theta_f$ is kept constant. The experimental data and $\bar{L}/\bar{D}$ computed from the model is shown in Figs. 10a–10d for $\Theta_f = 40°$ and in Figs. 10e–10h for $\Theta_f = 90°$. For both amplitudes, advanced flip ($\phi_r > 0°$) results in an increase of C_L and of $\bar{L}/\bar{D}$. The maximum values of $\bar{L}/\bar{D}$ occur at values of ϕ_r between 0 and 20°, whereas C_L increases almost linearly with ϕ_r.

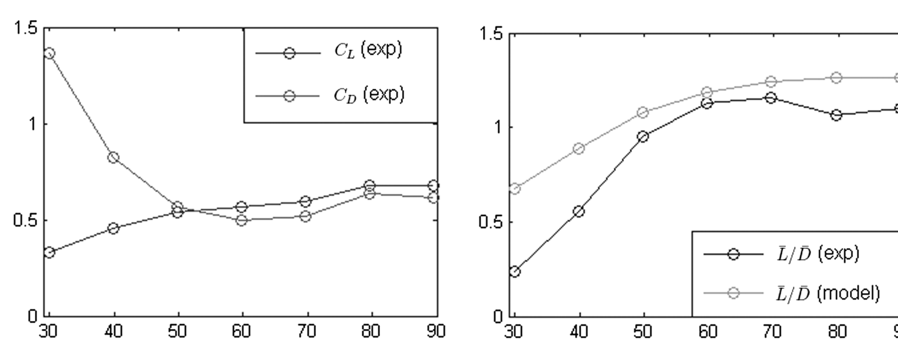

Fig. 7 Effect of varying Θ_f while maintaining constant Re, U_t, and denominators of C_L and C_D. The $\bar{L}/\bar{D}$ ratio and C_L increase as Θ_f is increased. The $\bar{L}/\bar{D}$ computed from the model shows a similar trend.

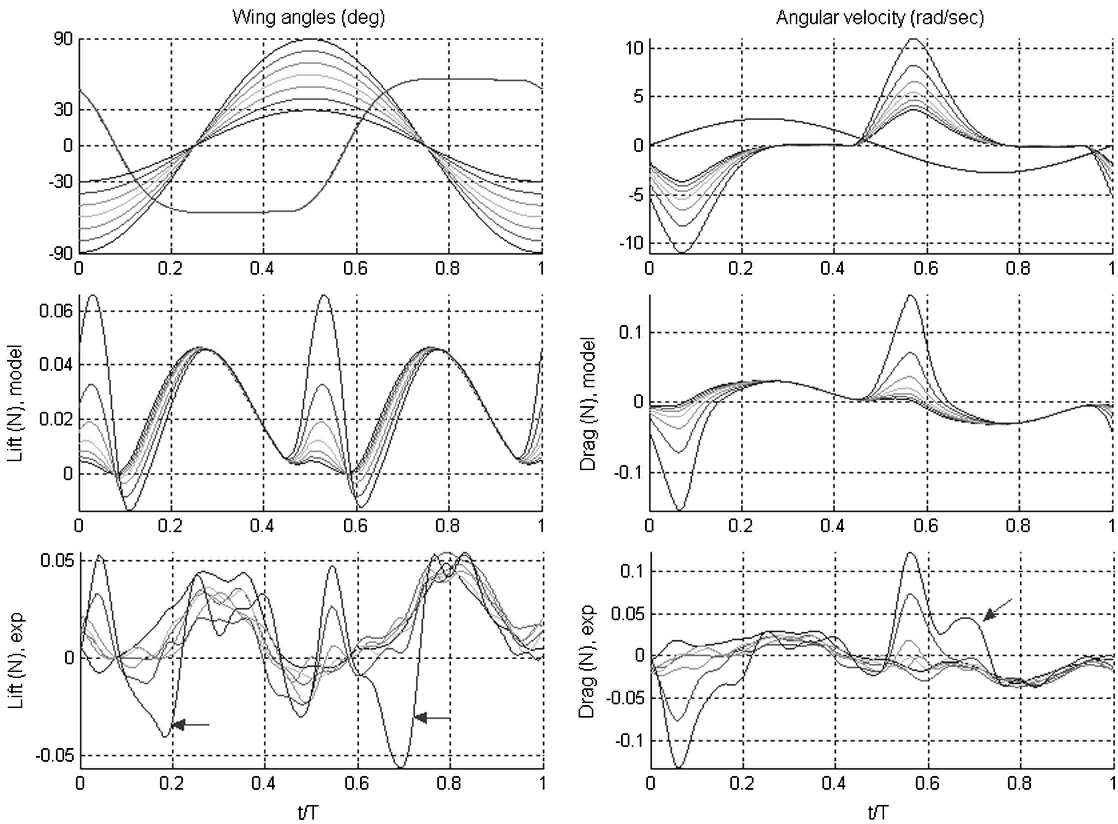

Fig. 8 Time trajectories of $L(t)$ and $D(t)$ over one wing-beat cycle for both model and experiment. Each curve is averaged over 10 wing-beat cycles. The experimental data show increased force peaks coinciding with wing rotation as Θ_f is decreased. The results also show secondary force transients at $\Theta_f = 30°$ (indicated by arrows), which are not predicted by the model. For this experiment, $\beta = 0°$, $\alpha_u = \alpha_d = 35°$, $\phi_r = 0°$, ΔT is nominal, $Re = 10,263$, and K varies from 0.1154 at $\Theta_f = 30°$ to 0.0385 at $\Theta_f = 90°$.

From Fig. 10, it can be seen that the aerodynamic performance is more sensitive to rotational motion at $\Theta_f = 40°$. In the case of $\Theta_f = 40°$, ΔT has a considerable effect on $\bar{L}/\bar{D}$. The slow flip results in a higher $\bar{L}/\bar{D}$ than with the fast and nominal flip durations. Both slow and nominal cases show improvement of C_L compared with the fast case. In the case of $\Theta_f = 90°$, ΔT has very little effect on C_L. whereas slow ΔT results in smaller $\bar{L}/\bar{D}$ values compared with the fast and nominal cases. The $\bar{L}/\bar{D}$ computed from the aerodynamic model matches less accurately in the case of $\Theta_f = 40°$, due to the large force peaks not captured by the model (see Fig. 8).

By varying ΔT and ϕ_r, we are able to improve $\bar{L}/\bar{D}$ and C_L for both $\Theta_f = 40$ and 90°, compared with the values of $\bar{L}/\bar{D}$ and C_L at the same amplitudes in Fig. 7. The maximum values of $\bar{L}/\bar{D}$ and C_L do not occur at the same ϕ_r, and a compromise must be made. A high C_L is important for carrying payload, whereas a high $\bar{L}/\bar{D}$ reduces aerodynamic power required for a given payload. Based on a requirement for high $\bar{L}/\bar{D}$, the most optimal operating point is $\Theta_f = 90°$, ϕ_r between 5 and 15°, and nominal ΔT.

D. Experiment 3: Optimal Angle of Attack α^*

Based on the results of experiments 1 and 2, we have established that C_L and $\bar{L}/\bar{D}$ increase at large Θ_f values, early flip ($\phi_r > 0°$), and nominal ΔT. However, α^* was kept constant at 35° during these experiments. In the third experiment, we maintain $\Theta_f = 90°$ and nominal ΔT, and $\alpha^* = \alpha_u = \alpha_d$ is varied from 10 to 70° in 5° increments. The experiment is repeated for five values of ϕ_r (−5, 0, 5, 10, and 15°), including the optimal range of ϕ_r found in the previous experiment.

The results given in Fig. 11 show that maximum $\bar{L}/\bar{D}$ occurs between $\alpha^* = 15$ and 20°; however, maximum C_L occurs at $\alpha^* = 55°$. Therefore, the optimal value of α^* is again a compromise between maximum $\bar{L}/\bar{D}$ and C_L. In hummingbirds and insects that hover with a horizontal stroke plane, α^* varies between 25 and 40° [5,18]. This gives a good compromise between C_L and $\bar{L}/\bar{D}$. For maximum desired $\bar{L}/\bar{D}$, α^* should be close to 25°, and for maximum desired C_L, α^* should be close 40°. The results again show that $\phi_r < 0°$ (delayed flip) decreases $\bar{L}/\bar{D}$ and C_L. The $\bar{L}/\bar{D}$ computed

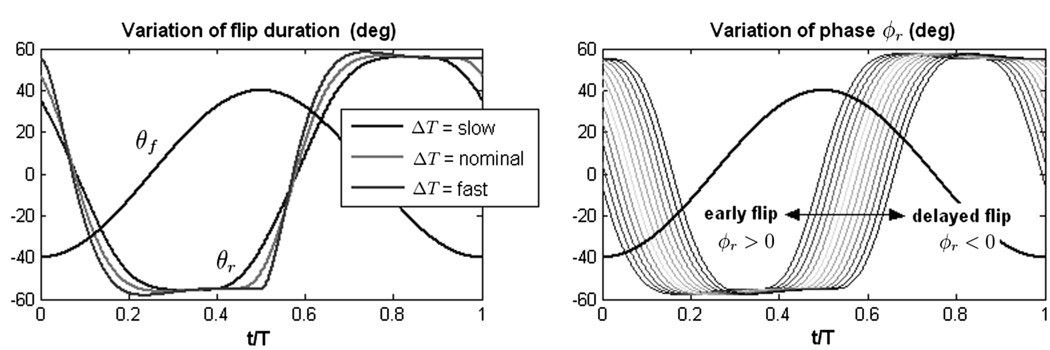

a) b)

Fig. 9 Variation in flip motion: a) perturbation in flip duration ΔT from nominal trajectory to fast and slow and b) for each flip duration, ϕ_r is varied from −30 to 30° in 5° increments. Note that $\phi_r > 0$ is an early flip, $\phi_r < 0$ is a delayed flip, and $\phi_r = 0$ is the nominal phase.

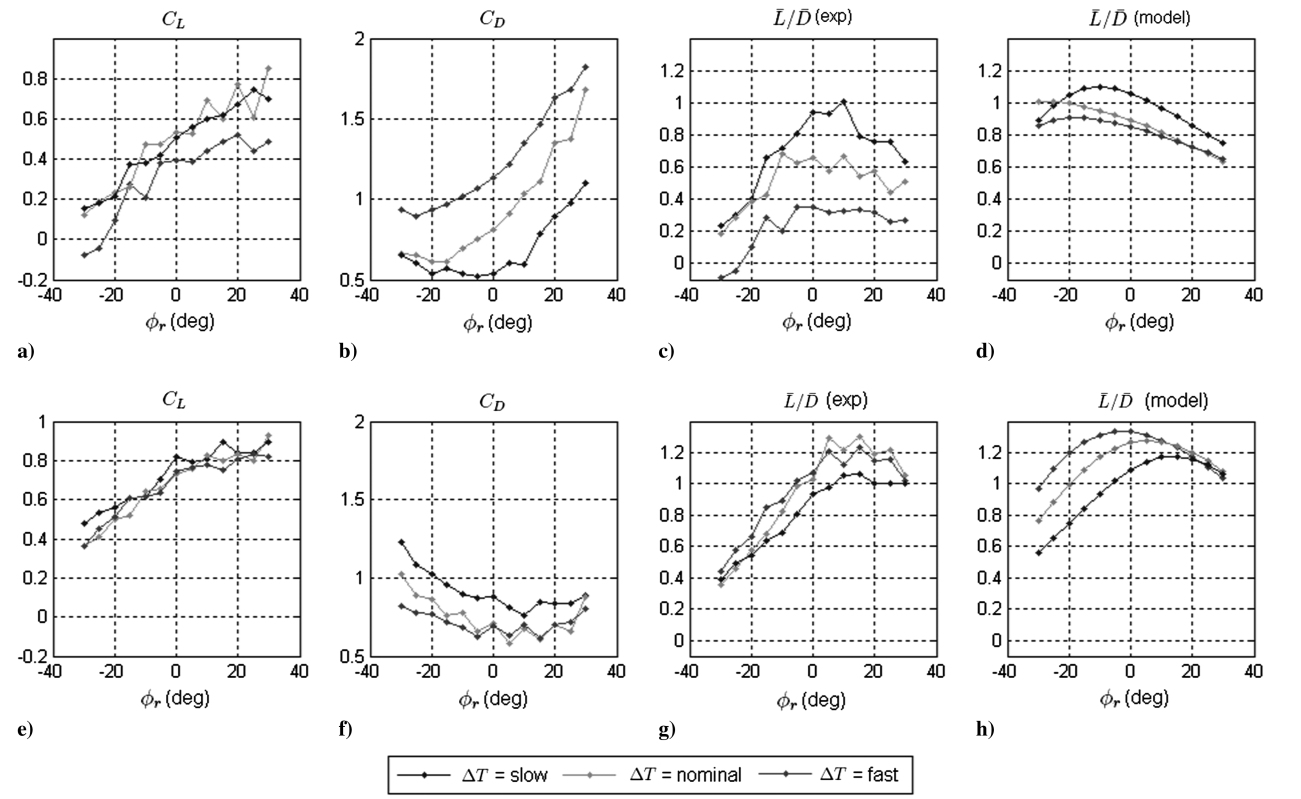

Fig. 10 Results of experiment 2: a–d) experimental data and $\bar{L}/\bar{D}$ computed from the model for $\Theta_f = 40°$, e–h) results for $\Theta_f = 90°$; $\beta = 0°$, $\alpha_u = \alpha_d = 35°$, and $Re = 18,326$; $K = 0.0865$ at $\Theta_f = 40°$ and $K = 0.0385$ at $\Theta_f = 90°$. See the text for an explanation of the results.

from the model is also shown and compares well with the experiment, except below $\alpha^* = 15°$, where experimental data show a very sharp decrease.

E. Experiment 4: Optimal Stroke-Plane Inclination β

In the previous three experiments, the stroke plane was kept horizontal: i.e., $\beta = 0°$. To determine the effect of stroke-plane inclination on optimal kinematics and aerodynamic performance, we used numerical optimization based on the aerodynamic model given by Eq. (5). The algorithm used for optimization is sequential quadratic programming, available as a `fmincon` function in MATLAB. In the case of an inclined stroke plane, the lift vector tilts forward by an angle β, since it is normal to the stroke plane. The vertical force F_v, which is transformed into the inertial frame $\mathcal{F}_o$ by Eq. (8), opposes gravity. Therefore, the $\bar{L}/\bar{D}$ ratio is modified to $\bar{F}_v/\bar{D}$, where

$$\bar{F}_v = \frac{1}{T}\int_o^T F_v(t)\,\mathrm{d}t$$

is the average vertical force over one wing-beat cycle. The cost function is given by

$$f(\Theta_f, \alpha_d, \alpha_u, \phi_r) = w_1\left(\frac{1}{\bar{F}_v}\right)^2 + w_2\left(\frac{\bar{D}}{\bar{F}_v}\right)^2 \tag{22}$$

where w_1 and w_2 are the weights. The cost function is independent of β; however, the optimization problem is solved for a range of β values, starting from 0° (horizontal stroke plane) to 90° (vertical stroke plane) in 10° increments. Furthermore, ΔT is fixed at nominal, which is optimal at $\Theta_f = 90°$ and $\beta = 0°$. This greatly simplifies the optimization problem. The cost function is designed to seek the optimal kinematic parameters that increase $\bar{F}_v$ and the $\bar{F}_v/\bar{D}$ ratio subject to the following constraints:

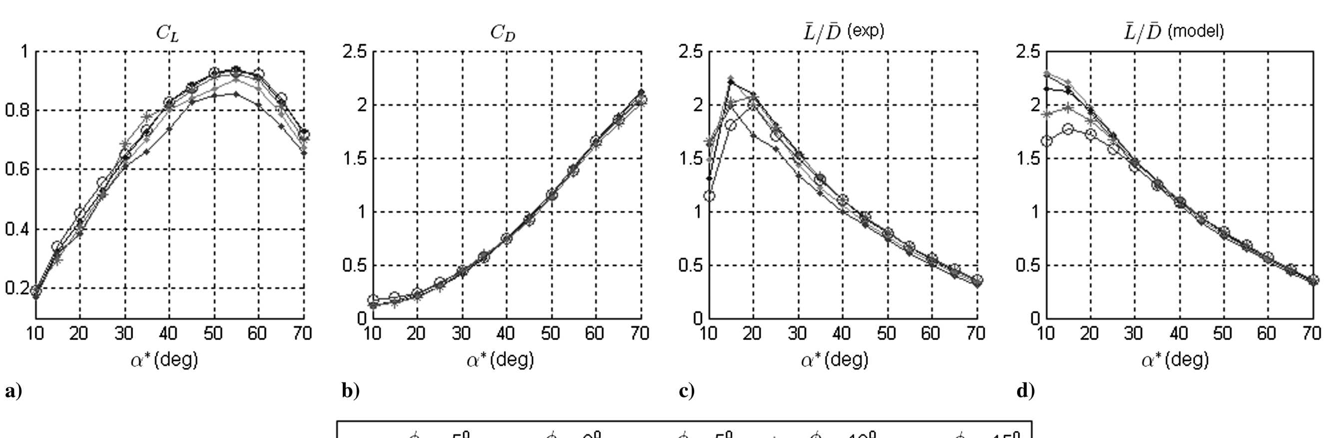

Fig. 11 Results of experiment 3. Plots of C_L, C_D, and $\bar{L}/\bar{D}$ against α^* are shown for five values of $\phi_r\,(-5, 0, 5, 10, 15°)$ at $\Theta_f = 90°$ and nominal ΔT. For this experiment, $Re = 18,326$ and $K = 0.0385$.

$$-\Theta_f < 0, \qquad \Theta_f - \pi/2 < 0 \tag{23}$$

$$\theta_r^d - \pi/2 < 0, \qquad -\theta_r^d < 0, \qquad -\theta_r^u - \pi/2 < 0, \qquad \theta_r^u < 0 \tag{24}$$

$$\phi_r - 30 < 0, \qquad -\phi_r - 30 < 0 \tag{25}$$

$$\bar{F}_h = \frac{1}{T}\int_0^T F_h(t)\,\mathrm{d}t = 0 \tag{26}$$

where the first two inequality constraints ensure that Θ_f remains between 0 and 90°. The next four inequality constraints ensure that wing rotation angle during downstroke remains between 0 and 90°, which is a feasible limit and similarly remains between 0 and $-90°$ during upstroke. The next inequality constraint keeps ϕ_r between -30 and 30°. Finally, the equality constraint ensures that the cycle-averaged horizontal force $\bar{F}_h$ in the inertial frame is zero. This is a fundamental requirement for hovering flight. $F_h(t)$ is computed from Eq. (8).

The cost function is weighted heavily toward increasing $\bar{F}_v/\bar{D}$ in a ratio of $w_2/w_1 = 3000$. The optimization results are shown in Fig. 12. For the case of the horizontal stroke plane ($\beta = 0°$), optimization gives $\Theta_f = 90°$, $\phi_r = 9.3°$, and $\alpha_u = \alpha_d = 24.3°$. These values are close to the values obtained in experiments 1, 2, and 3 for maximum $\bar{L}/\bar{D}$. As β is increased from 0 to 90°, the flap amplitude Θ_f decreases, ϕ_r shifts from positive to negative, and α_d increases almost linearly, whereas α_u decreases. At $\beta = 90°$, $\alpha_d \approx 90°$ during downstroke, offering maximum resistance, whereas $\alpha_u \approx 0°$ during upstroke, offering no resistance. The robotic flapper was operated at the optimal kinematics for each β value, and values of $\bar{F}_v$ and $\bar{F}_h$ and the $\bar{F}_v/\bar{D}$ ratio were obtained; these are shown in Figs. 12b and 12c, along with the values obtained from the model. The product $f\Theta_f$ is kept constant during this experiment, which means the coefficient of vertical force $C_v \propto \bar{F}_v$. Here, C_v replaces C_L and is obtained from Eq. (21) by substituting $\bar{F}_v$ for $\bar{L}$. The experimental results closely match the numerical optimization results. The hovering constraint $\bar{F}_h = 0$ is also nearly satisfied. The results show that the maximum $\bar{F}_v/\bar{D}$ occurs at $\beta = 0°$ and decreases considerably for increasing values of β. The average vertical force $\bar{F}_v$ (or C_v) is nearly the same for all β values. Therefore, the most optimal stroke-plane inclination is horizontal ($\beta = 0°$), along with the values of Θ_f, ϕ_r, α_u, and α_d determined above.

V. Feasibility of Passive Wing Rotation

The cycle-averaged aerodynamic power is computed by

$$\bar{P}_a = \frac{1}{T}\int_0^T P_a(t)\,\mathrm{d}t$$

where $P_a(t)$ is given by Eq. (10). The components of $\bar{P}_a$ are the averaged rotational power $\bar{P}_{\mathrm{rot}}$ and flapping power $\bar{P}_{\mathrm{flap}}$. In the thorax model, the wing rotation is generated passively. If we ignore the effects of wing inertia, stiffness, and friction, passive rotation requires that $\bar{P}_{\mathrm{rot}} < 0$. Therefore, to study the effect of wing kinematics on aerodynamic power and to check the feasibility of passive rotation, we computed $\bar{P}_a$, $\bar{P}_{\mathrm{rot}}$, and $\bar{P}_{\mathrm{flap}}$ for the data of experiments 2 and 3. Note that $\bar{P}_{\mathrm{rot}}$ reflects the rotational aerodynamic power mainly at the end of the stroke, when the wing flips. During the flapping phase, $\bar{P}_{\mathrm{rot}} \sim 0$, since wing rotation is negligible. Therefore, cycle-averaged rotational aerodynamic power is a good measure of the feasibility of passive wing rotation.

The plots of aerodynamic power for experiment 2 ($\Theta_f = 90°$ case) are shown in Figs. 13a–13c for the three flip durations against ϕ_r, ranging from -30 to 30° in 5° increments at $\alpha = 35°$. The optimal phase range ($5° < \phi_r < 15°$) that maximizes $\bar{L}/\bar{D}$ is indicated by the vertical lines in Fig. 13b (see also Fig. 10g). The power curves of experiment 2 show that $\bar{P}_a$ approaches minimum value in the optimal ϕ_r range and $\bar{P}_{\mathrm{rot}}$ comprises a tiny fraction of $\bar{P}_a$ for all ϕ_r values. In the optimal phase range, $\bar{P}_{\mathrm{rot}} < 0$ when ΔT is a slow curve and when ΔT is a nominal curve below $\phi_r = 12°$. When ΔT is a fast curve, $\bar{P}_{\mathrm{rot}} < 0$ below $\phi_r = -10°$, which is outside the optimal ϕ_r range. The results of experiment 2 in Fig. 10g show that the fast and nominal flip durations result in larger $\bar{L}/\bar{D}$ values, compared with the slow flip duration in the optimal ϕ_r range. Therefore, based on the feasibility of passive rotation, the most optimal operating region is given by the nominal ΔT case below $\phi_r = 12°$. For values of ϕ_r greater than 15°, higher C_L can be achieved, but passive rotation will not be feasible. The optimal phase range ($5° < \phi_r < 15°$) roughly lies between the infeasible region and the region of poor aerodynamic performance.

Similarly, Figs. 13d–13f show the aerodynamic power data for experiment 3, where the power curves for values of ϕ_r (-5, 0, 5, 10, and 15°) are plotted against α^*. The data show that $\bar{P}_a$ increases monotonically with α^* and almost identically for all ϕ_r values. $\bar{P}_{\mathrm{rot}}$ is again a tiny fraction of $\bar{P}_a$ for all α^* values and varies with increasing ϕ_r, as shown in Fig. 13e. The results of experiment 3 show that peak aerodynamic performance occurs at $\phi_r > 0°$, and the optimal angle of attack range is $25° < \alpha^* < 40°$, indicated by the vertical lines in Fig. 13e. However, $\bar{P}_{\mathrm{rot}} > 0$ for $\phi_r \geq 10°$ in the optimal α^* range, as shown in Fig. 13e. The curves for $\phi_r = 0$ and $-5°$ show that $\bar{P}_{\mathrm{rot}} < 0$ in the optimal α^* range, but the aerodynamic performance also decreases. Therefore, the most optimal and feasible operating region is $5° < \phi_r < 10°$ for values of $\alpha^* > 30°$. Therefore, the optimal range of α^* lies roughly between the infeasible region, where $P_{\mathrm{rot}} > 0$, and a region of poor aerodynamic performance.

These results show that the requirement of passive wing rotation limits the optimal solution. However, we did not take into account the effects of rotational inertia of the wing and strain energy of the rotational spring in this analysis. The center of mass of the wing is located behind the rotation axis (leading edge). Therefore, when the wing decelerates near the end of the stroke, the rotational component

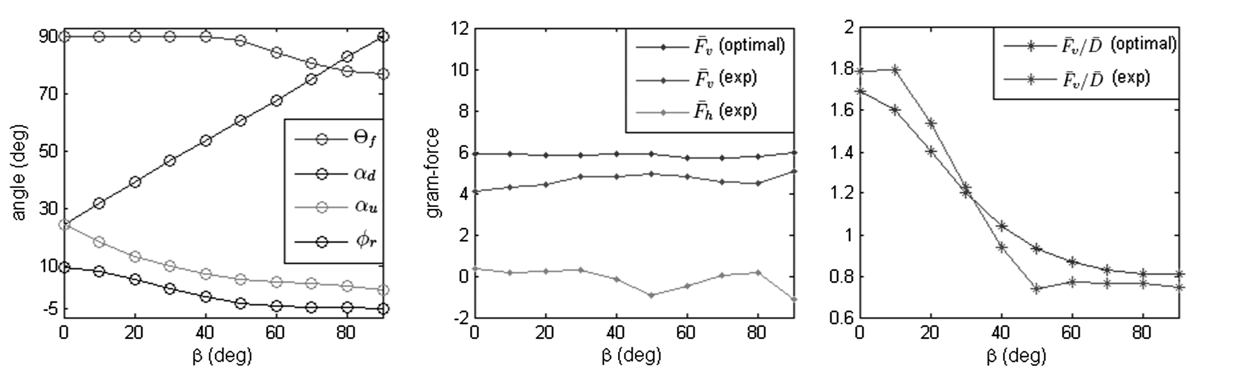

a) b) c)

Fig. 12 Optimization results: a) optimal values of Θ_f, α_d, α_u, and ϕ_r against β; b–c) values of $\bar{F}_v$, $\bar{F}_h$, and $\bar{F}_v/\bar{D}$ obtained from the model and experiment using the values of optimal kinematic parameters. The experimental result shows that $\bar{F}_h$ is close to zero for all β values. This verifies the optimization constraint $\bar{F}_h = 0$. Peak $\bar{L}/\bar{D}$ occurs at $\beta = 0°$, and $\bar{F}_v \propto C_v$ is the same for all β values.

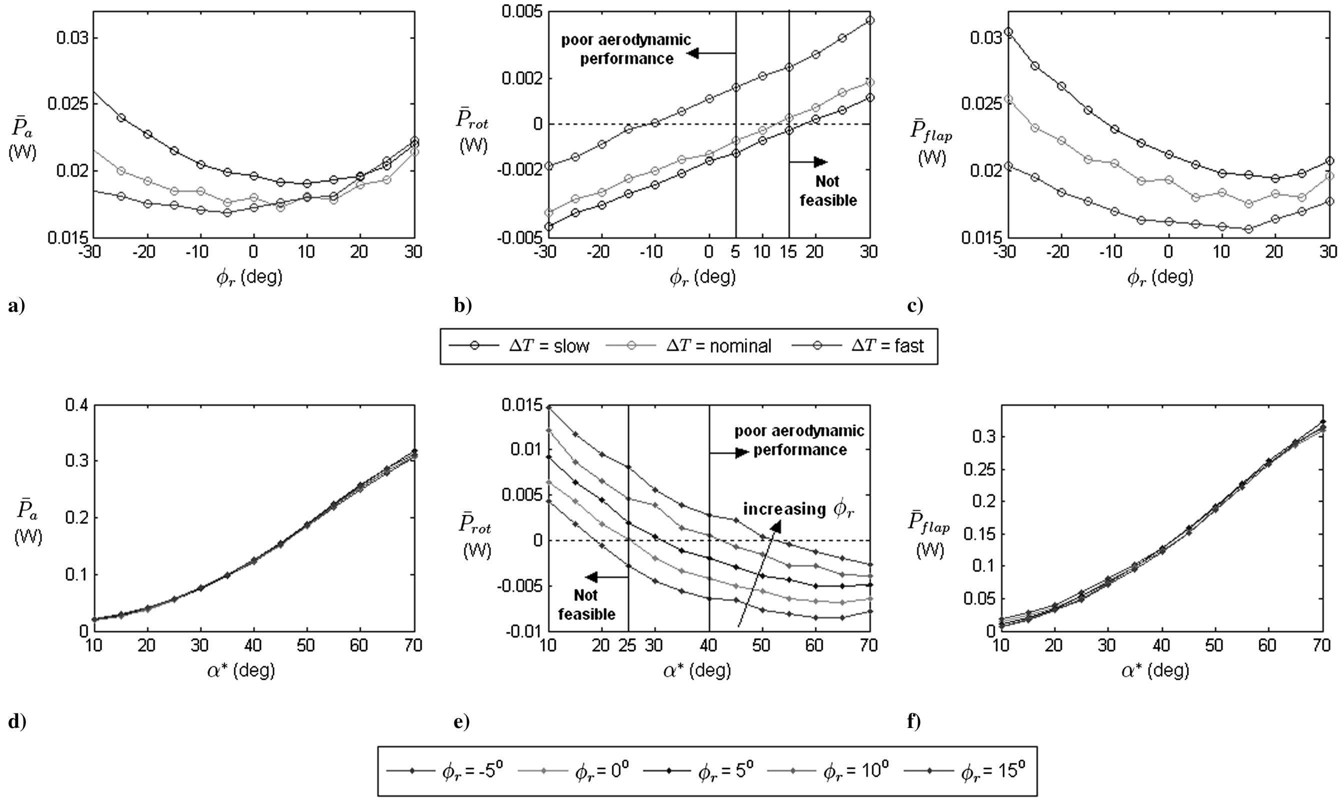

Fig. 13 Aerodynamic power data for a–c) experiment 2 and experiment d–f) experiment 3. $\bar{P}_a$ is the total aerodynamic power, which is the sum of rotational power $\bar{P}_{\mathrm{rot}}$ and flapping power $\bar{P}_{\mathrm{flap}}$. The results show that passive wing rotation is feasible in the optimal range of ϕ_r and α indicated by the vertical lines, since $\bar{P}_{\mathrm{rot}}$ is close to zero in this range.

of inertial power should be negative. If inertial power is added, the effect would be to shift the P_{rot} curves down and extend the feasible region [19].

VI. Conclusions

In this paper, a two-degree-of-freedom model of an insect thorax is presented along with an aerodynamic model of flapping wings. Despite the simplifying assumptions in modeling, computer simulations reveal insectlike kinematics. These kinematics can be described by a few parameters that can be varied without changing the kinematics qualitatively. Using experiments and numerical optimization, the optimal values of these kinematic parameters, along with other useful results, were found. These are summarized below.

1) Maximum averaged lift coefficient C_L and lift-to-drag ratio $\bar{L}/\bar{D}$ do not occur at the same parameter values. Therefore, a compromise has to be made between achieving maximum lift capability (high C_L) and maximum lift/drag (high $\bar{L}/\bar{D}$ ratio).

2) Large Θ_f increases both C_L and $\bar{L}/\bar{D}$. The maximum physical limit is $\Theta_f = 90°$, due to wings colliding with each other.

3) Advanced flip ($\phi_r > 0°$) increases both $\bar{L}/\bar{D}$ and C_L. However, although C_L increases almost linearly with ϕ_r, maximum $\bar{L}/\bar{D}$ occurs at $\phi_r \approx 10°$.

4) There exists an optimal flip duration ΔT that increases maximum $\bar{L}/\bar{D}$. However, ΔT has little effect on C_L.

5) Aerodynamic performance (C_L, $\bar{L}/\bar{D}$) is sensitive to rotational motion at smaller stroke amplitudes, where unsteady effects are maximum.

6) Maximum C_L occurs close to $\alpha^* = 55°$, and maximum $\bar{L}/\bar{D}$ occurs at $\alpha^* \approx 20°$. A good compromise can be achieved in the range of $25° < \alpha^* < 40°$.

7) Maximum $\bar{L}/\bar{D}$ occurs at $\beta = 0°$ (horizontal stroke plane).

8) The quasi-steady aerodynamic model becomes less accurate at smaller stroke amplitudes, where reduced frequency K is large.

9) Passive wing rotation is feasible for the optimal kinematics. Furthermore, the feasible region extends further if inertial effects are included.

The quasi-steady aerodynamic model used in this study depends upon the experimentally determined force and torque coefficients C_1, C_2, and C_{my}, which are a strong function of Reynolds number, wing geometry, and kinematics. Therefore, generic use of this aerodynamic model should be avoided. However, the model is not computationally intensive, and despite its limitations, it can be used for numerical optimization as done in this paper and for study of flapping-wing flight dynamics.

A future goal will be to determine the optimal parameters of the thorax model in order to generate the optimal kinematics. The thorax model parameters include wing inertia, flapping, rotational stiffness, and excitation frequency. This analysis might explain the significance of optimal wing inertia distribution and stiffness in improving aerodynamic performance. The thorax model can then be used as a conceptual model for the design of FWMAV flapping mechanism, in which the passive wing rotation can significantly reduce the mechanical complexity and weight of the device.

Acknowledgments

The authors gratefully acknowledge the funding of the National Science Foundation and the U.S. Army Research Office in support of this work (grant W911NF-05-1-0066).

References

[1] Wood, R. J., "The First Takeoff of a Biologically Inspired At-Scale Robotic Insect," *IEEE Transactions on Robotics and Automation*, Vol. 24, No. 2, April 2008, pp. 341–347. doi:10.1109/TRO.2008.916997

[2] Sane, S. P., and Dickinson, M. H., "The Control of Flight Force by a Flapping Wing: Lift and Drag Production," *Journal of Experimental Biology*, Vol. 204, 2001, pp. 2607–2626.

[3] Berman, G. J., and Wang, Z. J., "Energy-Minimizing Kinematics in Hovering Insect Flight," *Journal of Fluid Mechanics*, Vol. 582, 2007, pp. 153–168. doi:10.1017/S0022112007006209

[4] Altshuler, D. L., Dickson, W. B., Vance, J. T., Roberts, S. P., and Dickinson, M. H., "Short-Amplitude High Frequency Wing Strokes

Determine the Aerodynamics of Honeybee Flight," *PNAS*, Vol. 102, No. 50, Dec. 2005, pp. 18213–18218.
doi:10.1073/pnas.0506590102

[5] Ellington, C. P., "The Aerodynamics of Hovering Insect Flight. V. A Vortex Theory," *Philosophical Transactions of the Royal Society of London, Series B: Biological Sciences*, Vol. 305, 1984, pp. 115–144.
doi:10.1098/rstb.1984.0053

[6] Ennos, R. A., "The Kinematics and Aerodynamics of the Free Flight of Some *Diptera*," *Journal of Experimental Biology*, Vol. 142, 1988, pp. 49–85.

[7] Fry, S. N., Sayaman, R., and Dickinson, M. H., "The Aerodynamics of Hovering Flight in *Drosophil*," *Journal of Experimental Biology*, Vol. 208, 2005, pp. 2303–2318.
doi:10.1242/jeb.01612

[8] Weis-Fogh, T., "Quick Estimates of Flight Fitness in Hovering Animals, Including Novel Mechanisms for Lift Production," *Journal of Experimental Biology*, Vol. 59, 1973, pp. 169–230.

[9] Ennos, R. A., "A Comparative Study of the Flight Mechanism of *Diptera*," *Journal of Experimental Biology*, Vol. 127, 1987, pp. 355–372.

[10] Miyan, J. A., and Ewing, A. W., "How *Diptera* Move Their Wings: A Re-Examination of the Wing Base Articulation and Muscle Systems Concerned with Flight," *Philosophical Transactions of the Royal Society of London, Series B: Biological Sciences*, Vol. 311, No. 1150, Nov. 1985, pp. 271–302.
doi:10.1098/rstb.1985.0154

[11] Dudley, R., *The Biomechanics of Insect Flight, Form, Function and Evolution*, Princeton Univ. Press, Princeton, NJ, 2002.

[12] Wootton, R. J., 1992, "Functional Morphology of Insect Wings," *Annual Review of Entomology*, Vol. 37, 1992, pp. 113–140.
doi:10.1146/annurev.en.37.010192.000553

[13] Liu, H., Ellington, C. P., Kawachi, K., Van Den Berg, C., and Willmott, A. P., "A Computational Fluid Dynamic Study of Hawkmoth Hovering," *Journal of Experimental Biology*, Vol. 201, 1998, pp. 461–477.

[14] Ellington, C. P., "The Novel Aerodynamics of Insect Flight: Applications to Micro-Air Vehicles," *Journal of Experimental Biology*, Vol. 202, 1999, pp. 3439–3448.

[15] Usherwood, J. R., and Ellington, C. P., "The Aerodynamics of Revolving Wings. I," *Journal of Experimental Biology*, Vol. 205, 2002, pp. 1547–1564.

[16] Dickinson, M. H., Lehmann, F. O., and Sane, S. P., "Wing Rotation and the Aerodynamic Basis of Insect Flight," *Science*, Vol. 284, June 1999, pp. 1954–1960.
doi:10.1126/science.284.5422.1954

[17] Walker, J. A., "Rotational Lift: Something Different or More of the Same?," *Journal of Experimental Biology*, Vol. 205, 2002, pp. 3783–3792.

[18] Warrick, D. R., Tobalske, B. W., and Powers, D. R., "Aerodynamics of the Hovering Hummingbird," *Nature*, Vol. 435, No. 7045, June 2005, pp. 1094–1097.
doi:10.1038/nature03647

[19] Wang, Z. J., "Passive Wing Pitch Reversal in Insect Flight," *Journal of Fluid Mechanics*, Vol. 591, 2007, pp. 321–337.

P. Beran
Associate Editor